Membrane Insertion Pathway of Annexin B12: Thermodynamic and Kinetic Characterization by Fluorescence Correlation Spectroscopy and Fluorescence Quenching†

Yevgen O. Posokhov,‡ Mykola V. Rodnin,‡ Lucy Lu,§ and Alexey S. Ladokhin*,‡

Department of Biochemistry and Molecular Biology, Kansas University Medical Center, Kansas City, Kansas 66160-7421, and Department of Physiology and Biophysics, University of California at Irvine, Irvine, California 92612

Received November 7, 2007; Revised Manuscript Received February 28, 2008

ABSTRACT: Experimental determination of the free energy stabilizing the structure of membrane proteins in their native lipid environment is undermined by the lack of appropriate methods and suitable model systems. Annexin B12 (ANX) is a soluble protein which reversibly inserts into lipid membranes under mildly acidic conditions, which makes it a good experimental model for thermodynamic studies of folding and stability of membrane proteins. Here we apply fluorescence correlation spectroscopy for quantitative analysis of ANX partitioning into large unilamellar vesicles containing either 25% or 75% anionic lipids. Membrane binding of ANX results in changes of autocorrelation time and amplitude, both of which are used in quantitative analysis. The thermodynamic scheme describing acid-induced membrane interactions of ANX considers two independent processes: pH-dependent formation of a membrane-competent form near the membrane interface and its insertion into the lipid bilayer. Our novel fluorescence lifetime topology method demonstrates that the insertion proceeds via an interfacial refolded intermediate state, which can be stabilized by anionic lipids. Lipid titration measurements are used to determine the free energy of both transmembrane insertion and interfacial penetration, which are found to be similar, ~–10–12 kcal/mol. The formation of the membrane-competent form, examined in a lipid saturation experiment, was found to depend on the local proton concentration near the membrane interface, occurring with pK = 4.3 and involving the protonation of two residues. Our results demonstrate that fluorescence correlation spectroscopy is a convenient tool for the quantitative characterization of the energetics of transmembrane insertion and that pH-triggered ANX insertion is a useful model for studying the thermodynamic stability of membrane proteins.

Folding and bilayer insertion of constitutive membrane proteins are managed by multiunit translocon complexes. For nonconstitutive proteins (e.g., bacterial toxins, colicins, and some annexins), however, such insertion is achieved spontaneously, in response to changes in environment. Recent thermodynamic evidence indicates that the underlying physicochemical principles for these two processes are likely to be the same (*1–3*). Thus, deciphering these principles with the help of spontaneously inserting proteins is relevant to the larger problems of membrane protein folding and stability.

Annexins constitute a structurally conserved family of proteins implicated in a variety of membrane-related functions (*4*). Besides the well-documented Ca^{2+}-dependent binding to membrane interfaces, shared by most annexins, annexin B12 (ANX)[1] has been demonstrated to insert in a transmembrane (TM) conformation at acidic pH (*5, 6*). Recently, we have demonstrated that this transition is reversible (*7*), which made ANX an attractive model for studies of thermodynamic stability. Because the information on the stability of membrane protein structure in the native lipid environment cannot be obtained by the usual methods [e.g., thermal or chemical denaturation (*8*)], an alternative approach has been devised that allows useful thermodynamic information to be extracted from data on membrane partitioning of short soluble peptides (*9, 10*). Here we present a further development of this approach by examining the energetics of the pH-triggered transbilayer insertion of ANX by means of fluorescence correlation spectroscopy (FCS).

FCS measures intensity fluctuations of a small number of fluorescent molecules diffusing through a small focal volume.

† This research was supported by NIH Grant GM-069783.

* To whom correspondence should be addressed. Phone: 913-588-0489. Fax: 913-588-7440. E-mail: aladokhin@kumc.edu.

‡ Kansas University Medical Center.

§ University of California at Irvine.

[1] Abbreviations: ANX, annexin B12; dye-labeled or fluorescent ANX, single-cysteine mutant Q4C of ANX, labeled with either Alexa488 or Alexa647 dyes; ANX-134-NBD, ANX-162-NBD, ANX-221-NBD, and ANX-251-NBD, NBD-labeled single-cysteine mutants D132C, D162C, Q221C, and E251C of ANX; LysoUB, UniBlue-1-palmitoyl-2-hydroxy-*sn*-glycero-3-phosphoethanolamine; NBD, 7-nitrobenz-2-oxa-1,3-diazol-4-yl; FRET, Förster resonance energy transfer; LUV, large unilamellar vesicles; POPC, palmitoyloleoylphosphatidylcholine; POPG, palmitoyloleoylphosphatidylglycerol; 25PC:75PG and 75PC:25PG, mixtures of POPC and POPG that contain a molar percentage of the corresponding lipid specified by the number; TM, transmembrane; IF, interfacial; F_{MC}, fraction of membrane-competent ANX; ΔG, free energy of transfer from water to membrane; ΔG^{TM}, free energy of membrane insertion (transfer from water to TM state); ΔG^{IF}, free energy of IF membrane binding; τ, membrane surface potential; FCS, fluorescence correlation spectroscopy.

10.1021/bi702223c CCC: $40.75
Published on Web 04/12/2008

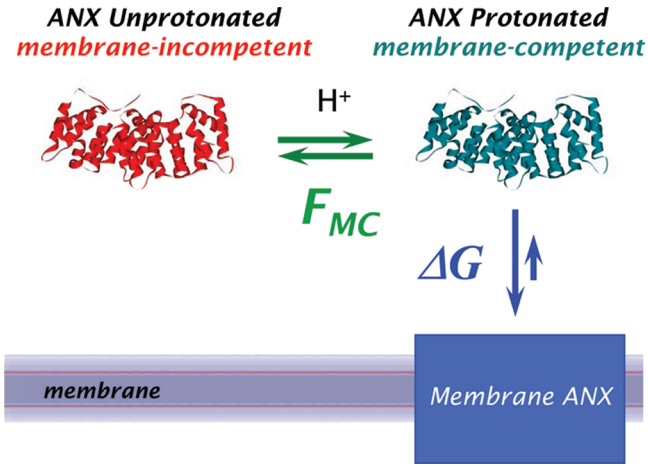

FIGURE 1: Thermodynamic scheme employed in the analysis of the energetics of pH-dependent membrane interactions of ANX. Acidification of ANX in solution (green arrows) leads to the formation of a membrane-competent form, which interacts with the lipid bilayer (blue arrows). Each of the two processes is characterized by an independent equilibrium parameter: the pH-dependent fraction of the membrane-competent form (F_{MC}) and the free energy of membrane partitioning of this form (ΔG). Both parameters, F_{MC} and ΔG, can be experimentally determined using FCS methodology.

Due to recent technical developments, FCS is gaining popularity in biological studies (*11*). Although this technique has not been applied yet to study transmembrane insertion of proteins, several groups have utilized it to study interfacial binding of peptides and proteins (*12, 13*). Rusu et al. (*12*) compared FCS results to those available from other measurements and found them to be in excellent agreement, opening the doors for quantitative application of FCS to membrane protein binding.

The thermodynamic scheme employed in the analysis of the pH-dependent membrane interactions of ANX contains two transitions (Figure 1): the formation of a membrane-competent form via protonation and its partitioning into the lipid bilayer. While presenting the FCS results, we use the terms "binding" and "partitioning" interchangeably to describe any mode of interaction with the membrane, including interfacial (IF) association and transmembrane (TM) insertion. FCS studies alone cannot distinguish the interfacial refolded intermediate state from the final transbilayer form of ANX. This is done by means of topology measurements based on fluorescence quenching methodology (*6, 14*). Both transitions depicted in Figure 1 are characterized by FCS to yield two independent equilibrium parameters: the pH-dependent fraction of the membrane-competent form (F_{MC}) and its free energy of membrane partitioning (ΔG). The latter is determined in a lipid titration experiment, while the former is estimated under lipid saturation conditions.

MATERIALS AND METHODS

Materials. Experiments at neutral and acidic pH were performed using 10 mM HEPES and 10 mM acetic acid buffers, respectively, both containing 1 mM EDTA and 50 mM KCl. Rhodamine 6G (Merck, Darmstadt, Germany) in buffer solution containing 100 mM NaCl and 10 mM HEPES, pH 7, was used for system calibration. POPC and POPG were obtained from Avanti Polar Lipids (Alabaster, AL). UniBlue A vinyl sulfone was purchased from Sigma (St. Louis, MO). INBD Alexa488-maleimide and Alexa647-maleimide were from Invitrogen (Carlsbad, CA). LysoUB was synthesized by covalently attaching the UniBlue A probe to the primary amino group of the lysoPE headgroup as previously described (*6*). The concentration of the stock solution was determined spectrophotometrically, assuming an extinction of 11000 M^{-1} cm^{-1} at 617 nm. NBD-labeled and Alexa-labeled annexin mutants were obtained by labeling single cysteine residues, as described previously (*6, 7*).

Sample Preparation for FCS. Large unilamellar vesicles (LUV) of diameter 0.1 μm were prepared by extrusion (*15, 16*). Lipid concentrations were determined according to the procedure of Bartlett (*17*). A single cysteine ANX mutant (Q4C) was labeled with either Alexa488 or Alexa647 dye as described previously (*7*). The labeling site, in the charged N-terminal domain, was chosen so as not to interfere with membrane interactions. Most of the experiments were performed with Alexa488, although the use of Alexa647 yielded identical results. The samples contained 0.5−6 nM dye-labeled ANX, which falls on the linear range for FCS concentration measurements, determined to be 6×10^{-8}−5×10^{-11} M for ANX-Alexa647 and 10^{-7}−4×10^{-10} M for ANX-Alexa488.

Experimental Setup. The experiment was conducted on a MicroTime 200 confocal microscope (PicoQuant, Berlin, Germany). The fluorescence was excited with pulsed picosecond diode lasers (LDH-P-C-470 for Alexa488 and LDH-P-C-635 for Alexa647) operated at 40 MHz. Narrow band cleanup filters ensured that no parasitic light reached the sample. The fluorescence was detected confocally after passing through emission band-pass filters (AHF/Chroma: HQ 520/40 for Alexa488, HQ 685/70m for Alexa647) blocking the excitation wavelength. In order to suppress influences from the afterpulsing typically observed with single photon avalanche diodes (SPAD), the fluorescence light was split with a 50/50 beam splitter cube onto two SPADs (SPCM-AQR-14; Perkin-Elmer Inc.), and cross-correlation analysis was applied. The high numerical aperture apochromatic water immersion objective (60×, NA 1.2; Olympus), together with the 50 μm confocal pinhole, resulted in a confocal detection volume of 0.5 fL. The confocal detection volume was calculated using calibration with a 5 nM Rhodamine 6G solution [diffusion constant $D_{Rh6G} = 2.8 \times 10^{-10}$ m^2 s^{-1} (*57*)]. The structural parameter S (eq 1) was determined from measurements with Rhodamine 6G to be 5.1, and the focus volume was found to be 0.4 fL. The fluorescence was detected by applying time-correlated single photon counting (TCSPC) with the TimeHarp 200 board. The data were stored in the time-tagged time-resolved mode (TTTR), which allowed the recording of every detected photon with its individual timing and detection channel information. The presented measurement was performed 200 μm deep in the solution with a total acquisition time of 30 s. The data were averaged from at least six measurements.

FCS Data Analysis. The autocorrelation function for single diffusing species undergoing Brownian motion can be described with the equation (*12, 18*):

$$G(\tau) = \frac{1}{N} g(\tau) = \frac{1}{N}\left(1 + \frac{T}{1-T} e^{-\tau/\tau_{Tr}}\right)\left(\frac{1}{1+\tau/\tau_D}\right)\left(\frac{1}{1+\tau/S^2\tau_D}\right)^{1/2} \quad (1)$$

where N is the average number of fluorescent molecules in

the focus volume and τ_D is the correlation time of the particles. The correlation time represents the diffusion time through the focus volume and equals $\tau_D = \omega^2/4D$, where ω^2 is the square of the radius of the laser focus and D is the diffusion constant. S is the ratio of the distances from the center of the laser beam focus in the radial and axial directions, respectively. T is the fraction of fluorophores in the triplet state and τ_{Tr} is the triplet lifetime ($\sim$2 μs in our case).

The measured correlation function $G(\tau)$ of a multicomponent system is a weighted sum of the autocorrelation functions of each component $G_i(\tau)$ with amplitudes A_i (*12, 13, 19*) as

$$G(\tau) = \sum_{i=1}^{M} q_i^2 N_i^2 G_i(\tau) \Big/ \left[\sum_{i=1}^{M} q_i N_i\right]^2 = \sum_{i=1}^{M} q_i^2 N_i g_i(\tau) \Big/ \left[\sum_{i=1}^{M} q_i N_i\right]^2 = \sum_{i=1}^{M} A_i g_i(\tau) \quad (2)$$

where N_i is the mean particle number and q_i is the ratio of the fluorescence yield of the ith component to that of the first component. In our system $q_i = 1$, as binding of dye-labeled ANX to vesicles does not change fluorescence intensity of either Alexa488 or Alexa647 fluorophores. For our system (ANX binding to LUV) we consider only two diffusing species: the fluorescently labeled proteins (index P) and LUV with bound fluorescently labeled proteins (index V):

$$G(\tau) = A_P g_P(\tau) + A_V g_V(\tau) \quad (3)$$

Determination of Membrane Partitioning from FCS Data. Information on the fraction of free and bound ANX can be extracted from the values of weighting factors in two different ways, depending on certain assumptions. First, we consider the case where each vesicle contains no more than a single bound protein, which will require an overwhelming molar excess of lipid ($\sim 10^6$), and is therefore referred to as an "infinite dilution regime". It also requires that the protein be the monomer (which is the case for ANX under the conditions of our FCS experiment (*7*)) or, at least, that the number of subunits in the oligomer is known. In this case the number of particles associated with the slow mobility will be equal to the number of vesicle-bound protein, and the fraction of bound protein will be equal (*19*):

$$\frac{[P]_{bound}}{[P]_{total}} = \frac{A_V}{A_V + A_P} \quad (4A)$$

In many cases, however, the infinite dilution regime is unachievable, and every vesicle carries several bound proteins, and eq 4A will no longer be valid. Nevertheless, as demonstrated by Rusu and co-workers (*12*), the fraction of bound protein/peptide still can be calculated from the FCS experiment, in this case by comparing measurements in the presence and in the absence of LUV. The autocorrelation collected in the presence of LUV is used to determine the amplitude associated with the free protein (A_P) by fitting the data with eq 3. The autocorrelation for the sample containing the same amount of protein, but no LUV, will be fitted with eq 1 to determine the total number of proteins/peptides in the focal volume (N). The fraction of the bound protein will be equal (*12*):

$$\frac{[P]_{bound}}{[P]_{total}} = 1 - A_P N \quad (4B)$$

The fraction of bound ANX as a function of lipid concentration is estimated depending on experimental conditions discussed above using either eq 4A or eq 4B. The resulting titration isotherm is fitted to a mole fraction partitioning equation (*9, 20*), modified to account for the presence of membrane-incompetent protein species (Figure 1):

$$\frac{[P]_{bound}}{[P]_{total}} = F_{MC}\frac{K_x[L]}{[W] + K_x[L]} \quad (5)$$

$$\Delta G = -RT \ln K_x$$

where F_{MC} is a fraction of membrane-competent ANX (determined at lipid saturation), [L] is lipid concentration, [W] is water concentration (55.3 M), and K_x is a mole fraction partitioning coefficient which is used to determine the free energy of binding ΔG.

Analysis of the pH Dependencies of F_{MC}. The fractions of bound ANX at lipid saturation were fitted to the equation:

$$F_{MC} = \frac{1}{1 + 10^{n(pH - pK)}} \quad (6)$$

where pK is the negative logarithm of the dissociation constant and n is the Hill coefficient. The pH values at membrane interfaces were calculated from bulk pH values and membrane surface potential (φ) (*21*):

$$pH_{interface} = pH_{bulk} - F\varphi/RT \quad (7)$$

where F and R are Faraday and gas constants, respectively, and T is the absolute temperature.

Time-Resolved Fluorescence Measurements and Membrane Topology Analysis. Fluorescence decays were measured with a time-resolved fluorescence spectrometer FluoTime 200 (PicoQuant, Berlin, Germany) using a standard time-correlated single-photon counting scheme as described in ref *14*. Samples were excited at 439 nm by a subnanosecond pulsed diode laser LDH 440 (PicoQuant, Berlin, Germany) with a repetition rate of 10 MHz. Fluorescence emission was detected at 536 nm, selected by a Sciencetech Model 9030 monochromator, using a PMA-182 photomultiplier (PicoQuant, Berlin, Germany). To reject the scattered light, the emission was recorded via a cut-on glass filter at 480 nm and a polarizer set at 54.7°. Data were normally collected to a constant peak value of 10000 counts. The instrumental response function (IRF) was recorded under the same conditions at the excitation wavelength by replacing the sample with a scattering solution of colloidal silica (LUDOX, Grace). The total width on the half-height of the IRF was about 0.3 ns. The samples normally contained 0.1 μM protein and 0.4 mM lipid. LysoUB was added from the micellar suspension in buffer either after 10 min or after 2 h of incubation of protein and LUV. Lifetime measurements took 2–3 min and were taken in 2 min after addition of LysoUB to minimize spontaneous translocation of the quencher across the bilayer.

The fluorescence intensity decay was analyzed using FluoFit software (PicoQuant, Berlin, Germany). The program uses an iterative fitting procedure based on the Marquardt algorithm to minimize the deviation of the experimental data,

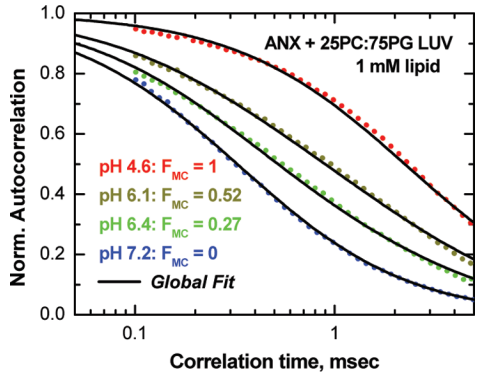

FIGURE 2: Example of binding measurement using FCS performed under conditions of the "infinite dilution regime" satisfied at extremely high lipid excess over fluorescently labeled protein (see Materials and Methods). Acidification results in a progressive shift of mobility from that of the free ANX (correlation time ~0.34 ms) to that of a vesicle-bound ANX (correlation time ~2.1 ms). Quantitative determination of partitioning is achieved by a linked analysis (solid lines) of fluorescence autocorrelation curves (dashed lines) that links the two correlation times for all curves and allows free fitting of the preexponential amplitudes (see eq 3). Note that the absolute values of amplitudes are not important under these conditions, but only their relative contributions (eq 4A). To indicate this fact and for the purpose of better visual representation, all data are normalized to the same number of fluorescent particles in the focal volume ($N = 1$).

presented as the sum of the three exponential components, the longest of which, τ, was used for topology analysis (*14*).

RESULTS

Before investigating the pH-dependent insertion of ANX, we tested the sensitivity of the FCS-based detection of membrane binding using the well-studied phenomenon of calcium-dependent binding of ANX to membrane interfaces (*4*). As expected, addition of Ca^{2+} resulted in a pronounced increase in the autocorrelation decay time of the dye-labeled ANX from 0.3 to 2.1 ms, which can be reversed by the addition of EGTA (not shown). This shift, resulting from the lower mobility of a relatively large vesicle (~100 nm diameter) compared to a free ANX molecule, is sufficient to make single color autocorrelation measurements useful for binding studies. Because the mobility of ANX bound to the vesicle in a Ca^{2+}-dependent manner and that of the ANX inserted into the vesicle at low pH are the same (they coincide with the mobility of the vesicle itself), we can use these results as the hallmarks for subsequent experiments at low pH.

FCS Experiments at Lipid Saturation. Next, we examined low pH insertion of ANX using a very dilute protein sample (1 nM) and a relatively high lipid concentration (1 mM), which serves two purposes. First, lipid saturation shifts the membrane-binding equilibrium toward the bound ANX, thus leaving the membrane-incompetent form as the only form of ANX in solution (Figure 1). Second, high lipid excess allows us to work in a so-called infinite dilution regime, which simplifies quantitative analysis of binding from FCS data (see Materials and Methods section). The example of such an experiment presented in Figure 2 reveals a progressive shift of the autocorrelation curve upon lowering the pH, consistent with progressive binding of ANX to vesicles. The diffusion time measured at pH 7.2 coincided with that of ANX in the absence of vesicles, while one measured at pH

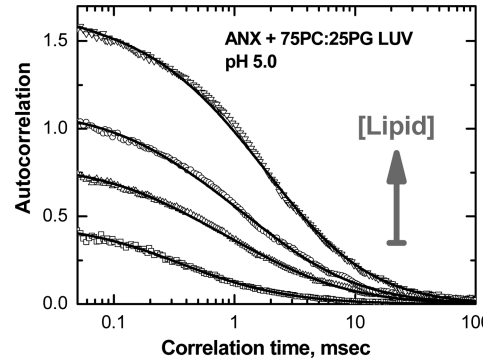

FIGURE 3: Example of binding measurement using FCS performed outside of the "infinite dilution regime" (the average number of ANX bound per vesicle is >1). Correlation curves (symbols) were measured for samples containing 1 nM ANX and no LUV or LUV with 1, 2, and 4 μM total lipid LUV (bottom to top). Progressive vesicle binding of fluorescently labeled ANX results in a reduction of the number of fluorescent particles in the focal volume and a corresponding increase in total autocorrelation amplitude. Solid curves correspond to a fit with eq 3 (or eq 1 for sample containing no LUV). The fractions of bound ANX are calculated by comparing absolute amplitudes in the presence and absence of LUV (eq 4B) and for data presented equal to 0, 0.42, 0.59, and 0.73 (bottom to top).

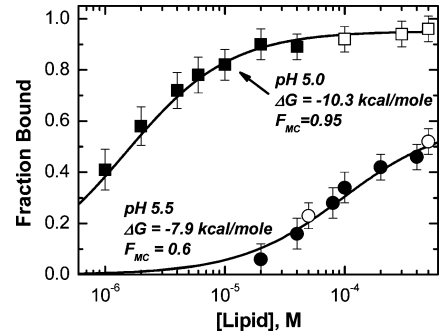

FIGURE 4: Typical ANX membrane-binding isotherms measured with 75PC:25LUV at pH 5.5 (circles) and pH 5 (squares). Closed symbols correspond to the experimental scheme described in Figure 2 (regular regime). Open symbols correspond to the experimental scheme described in Figure 3 (infinite dilution regime). Solid curves are the fitting results using eq 5 with the corresponding parameters presented on the graph. Note that both parameters, the fraction of the membrane-competent form F_{MC} and the free energy of membrane partitioning ΔG, are pH-dependent.

4.6 coincided with that of totally bound ANX in the Ca^{2+}-triggered binding experiment. Thus, the limiting curves in Figure 2 can be assigned to a totally free and totally membrane-bound ANX. This assignment allowed us to determine the fractions of free and bound protein at intermediate pH using the global (or linked) analysis approach (*22, 23*). Specifically, the diffusion times for free and bound ANX were linked for all four curves, while the fractions of free and bound ANX for the two middle curves were allowed to float. The resulting global fit (solid curves) is rather good and provides accurate determination of the bound fractions.

The final results from lipid saturation experiments for two lipid systems are presented in Figure 5A (open symbols). We confirm that our experimental conditions indeed correspond to lipid saturation by reducing lipid concentration in half, which did not result in any change in the fractions of free and bound ANX (not shown). Therefore, the data plotted in Figure 5A present the pH-dependent formation of

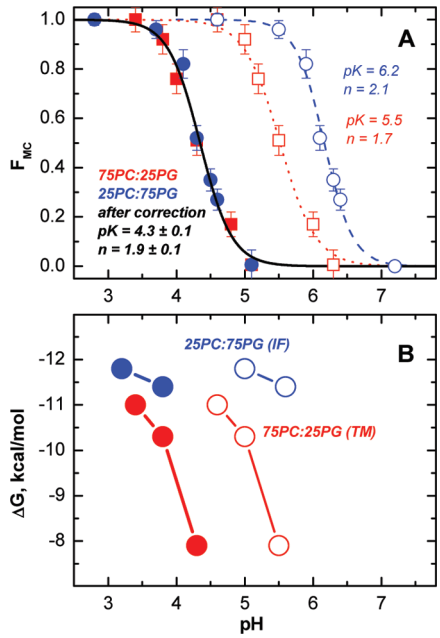

FIGURE 5: Summary of thermodynamic parameters characterizing the pH-dependent membrane insertion pathway of ANX. Red and blue symbols correspond to 75PC:25PG and 25PC:75PG lipid compositions, respectively. The same data sets are plotted using either uncorrected bulk pH values (open symbols) or corrected pH values near the membrane interfaces with different surface potentials (closed symbols). Corrected pH dependences for the formation of the membrane-competent form (A) measured with the two lipid compositions coincide (solid squares) and can be fitted with a single curve using eq 6 (black line). The resulting parameters suggest that the conversion to a membrane-competent form requires protonation of two residues ($n \sim 2$). The free energies of membrane partitioning (B) depend on the pH and lipid composition, which are known to affect the insertion of the ANX. PC-rich LUV (75PC:25PG) promote fast insertion of ANX into the transmembrane (TM) state, while PG-rich LUV (25PC:75PG) stabilize an interfacial (IF) intermediate state (see Discussion).

the membrane-competent form and can be fitted with eq 6 to determine the effective pK and the Hill coefficient n. The latter was found to be similar for the two lipid compositions used in this study: 1.7 ± 0.2 for 75PC:25PG and 2.1 ± 0.2 for 25PC:75PG. The corresponding pK's, however, differ substantially: 5.5 ± 0.2 for 75PC:25PG and 6.2 ± 0.1 for 25PC:75PG. This difference for the apparent protonation behavior in solution (presumed to be lipid-independent) is surprising only at first glance. In reality, formation of the membrane-competent form is likely to occur near the membrane interface, where local proton concentration is different from that in the bulk solution. Moreover, local proton concentration will be different for the two lipid compositions because of the difference in the surface potential. We correct for this difference using eq 7 (*21*) and replot the same data, now using corrected pH values (Figure 5A, solid symbols). Surprisingly, this rather simple correction gives excellent results as the data sets for both lipids coincide, as they should. The combined data set is fitted with eq 6 (black line), and the following parameters are obtained: pK = 4.3 ± 0.1; n = 1.9 ± 0.1.

FCS Lipid Titration Experiments. In order to obtain information on the energetics of membrane portioning of the protonated membrane-competent ANX, one needs to examine the fraction of free and bound ANX as a function of the lipid concentration. As a rule, such experiments cannot be done under conditions of infinite dilution, and the assumptions for the simplified analysis (eq 4A) are no longer valid. We circumvent this problem by following the example of Rusu et al. (*12*), who estimated free and bound fractions by comparing autocorreltion amplitudes for samples of the same protein concentration in the presence and in the absence of LUV (see also Materials and Methods). An example of such an analysis is presented in Figure 3: symbols are experimental autocorrelation curves and the solid lines are fitting results with eq 3 (or eq 1 in case of no LUV sample). Addition of increasing concentrations of LUV results in progressive membrane binding and reduction in concentration of free ANX. This leads to an overall reduction in the number of fluorescent particles (free ANX plus vesicle with bound ANX), since under these conditions a single vesicle carries more than a single labeled protein. The average number of particles in the focal volume is inversely proportional to the autocorrelation amplitude. Therefore, the amplitude is expected to increase with increasing lipid concentration, which is indeed observed (Figure 3). The quantitative analysis of binding is based on fitting individual curves to a two-component autocorrelation function (eq 3, solid lines) and extracting the fractions of bound ANX by comparing relative amplitudes in the presence and absence of LUV (see Materials and Methods and eq 4B).

Two examples of the resulting titration isotherms collected with 75PC:25PG LUV at pH 5.0 and 5.5 are shown in Figure 4. Several data points collected under infinite dilution conditions (open symbols) fall on the same curve, which confirms the validity of our FCS treatment under these conditions. Solid symbols correspond to the analysis outlined above, with the lines representing a two-parameter fit with eq 5 describing our thermodynamic scheme in Figure 1. Both fitting parameters vary with the change of pH, with F_{MC} mirroring the difference observed in lipid saturation experiments. The ΔG values obtained by this analysis for the two lipid systems studied here are summarized in Figure 5B and range up to 12 kcal/mol.

Experimental and Computational Analysis of Topology. The final inserted state of ANX is believed to be an aqueous pore, comprised of several TM helices, very few of which have been identified experimentally (*5, 6, 24*). Hydropathy analysis of ANX at low pH (e.g., glutamic, aspartic, and histidine residues are assumed to be protonated) with the web-based tool MPEx identifies several potential TM segments, centered at residues 146, 243, and 301 (black bars in Figure 6). The first one coincides with the E−D region of repeat 2 that was experimentally demonstrated to cross the bilayer (*5, 6*). Previously, we have demonstrated the insertion of a C-terminal part of this segment across the bilayer in the final TM conformation, using our steady-state fluorescence LysoUB topology method (*6*).

We have applied our lifetime fluorescence-based topology method (*14*) to examining the translocation of several critical sites on the ANX sequence during pH-triggered insertion. Four single-cysteine mutants (D132C, D162C, Q221C, E251C) were labeled with NBD dye as described before (*6*) and mixed with extruded large unilamellar vesicles (LUV) containing various amounts of anionic POPG and zwitterionic POPC lipids at pH 4.6 in the presence of 1 mM EGTA to remove Ca^{2+}. The LysoUB quencher, comprised of a UniBlue FRET quencher of NBD and a single acyl chain,

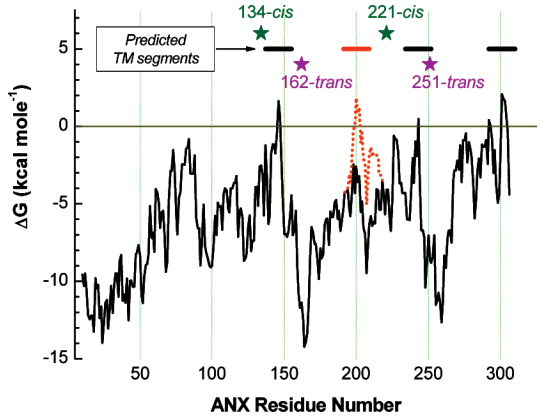

FIGURE 6: Hydropathy analysis of ANX with the web-based tool MPEx (S. Jaysinghe, K. Hristova, W. Wimley, C. Snider, and S. H. White (2006) http://blanco.biomol.uci.edu/mpex) using a standard low pH assumption (black line) and additional deprotonation of H205 and H209 (orange line). The pattern of predicted TM segments (bars) is compared to *cis* or *trans* topology experimentally determined at several sites (stars). See text for details.

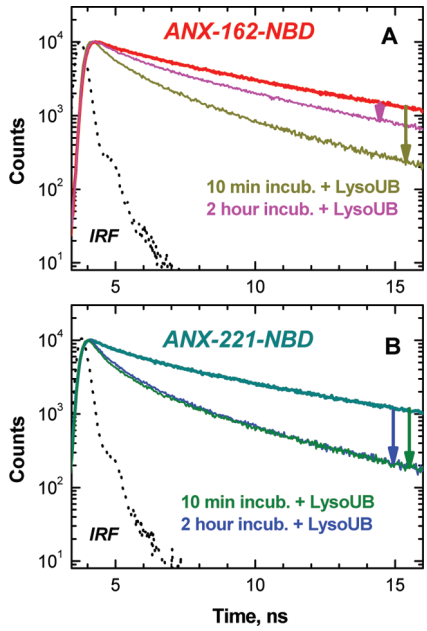

FIGURE 7: Typical fluorescence decay experiment used to determine the topology of the NBD probe attached to ANX residue 162 (A) or residue 221 (B) 25PC:75PG LUV. Arrows illustrate the amount of quenching caused by addition of 2% LysoUB after 10 min or 2 h of the initiation of protein insertion. Strong quenching indicates the *cis* location of the probe (e.g., ANX-221-NBD or ANX-162-NBD after 10 min incubation with 25PC:75PG LUV). Translocation of the protein-attached NBD across the bilayer results in reduced quenching (e.g., ANX-162-NBD after 2 h incubation). The topology assignments for several ANX mutants under various experimental conditions based on the quantitative results of the lifetime quenching experiments are presented in Table 1.

was added to a 2% level of the total lipid from aqueous micellar stock. Fluorescence decays were measured after either 10 min or 2 h incubation of NBD-labeled ANX with LUV (Figure 7, coinciding top lines), after which a LysoUB quencher was added and fluorescence decays were measured (lower lines). (Note that in all cases, in order to minimize the translocation of LysoUB across the bilayer by inserting protein, the quencher was added from aqueous stock 2 min prior to data acquisition.) The arrows, presented in the graphs, serve to visualize the amount of quenching. Large quenching

Table 1: Experimental Determination of *Cis* or *Trans* Topology of Several NBD-Labeled Sites of ANX during pH-Triggered Membrane Insertion[a]

labeled residue	LUV	incubation	τ_0/τ	topology
134	25POPC:75POPG	10 min	1.50	*cis*
		2 h	1.51	*cis*
	75POPC:25POPG	10 min	1.48	*cis*
		2 h	1.47	*cis*
162	25POPC:75POPG	10 min	1.60	*cis*
		2 h	1.29	*cis/trans*
	75POPC:25POPG	10 min	1.19	*trans*
		2 h	1.11	*trans*
221	25POPC:75POPG	10 min	1.60	*cis*
		2 h	1.66	*cis*
	75POPC:25POPG	10 min	1.57	*cis*
		2 h	1.63	*cis*
251	25POPC:75POPG	10 min	1.48	*cis*
		2 h	1.41	*cis/trans*
	75POPC:25POPG	10 min	1.25	*trans*
		2 h	1.23	*trans*

[a] Analysis details were described previously (*14*) and in the text.

corresponds to the *cis* location of the NBD-labeled site; low quenching corresponds to the *trans* location. Even prior to any mathematical analysis of the fluorescence decay, our raw data indicate that some mutants (e.g., ANX-221-NBD, Figure 7B) demonstrate a constant and high level of quenching, while the others (e.g., ANX-162-NBD, Figure 7A) show incubation-dependent reduction in quenching. The latter indicates time-dependent insertion, while the former indicates that the labeled site remains on the *cis* side of the bilayer at all times during the insertion. Thus, this new lifetime-based methodology allows us to directly detect a *cis*-located intermediate state populated at early incubation times. As far as we know, this is the first direct kinetic measurement of topology for any membrane protein.

In order to describe LysoUB quenching, and the resulting topology, in a quantitative way, we have analyzed the fluorescence decay for all samples and calculated the ratio of the long lifetime component upon addition of the quencher, as described previously (*14*). Comparison of the quenching in well-defined model systems indicates that the ratio of the longest decay time in the absence (τ_0) and presence of 2% LysoUB (τ) is sensitive to the topology of the NBD-labeled site: (a) weak quenching ($\tau_0/\tau \leq 1.25$) indicates translocation to the *trans* side of the bilayer, (b) strong quenching ($\tau_0/\tau \geq 1.45$) indicates lack of translocation, and (c) intermediate quenching is consistent with a mixture of *cis* and *trans* locations of the probe (*14*). The topology assignments of various sites of the ANX were made by comparison with these hallmarks (Table 1). Our data indicate that the NBD-labeled sites at residues 134 and 221 give a very robust decrease in lifetime upon quenching and therefore are not translocated. (In addition, the strong quenching observed with ANX-221-NBD and ANX-134-NBD serves as a control for the absence of the spontaneous translocation of the LysoUB to the inner leaflet on the experimental time scale.) In contrast, sites at residues 162 and 251 show great variations in quenching, depending on time of incubation and lipid composition. Membranes with high POPG content appear to favor a nontranslocated state. Residues 162 and 251, however, are translocated in the final structure already after 10 min incubation with 75PC:25PG membranes that favor translocation (Table 1). These results confirm our early suggestion as to the existence of a kinetic insertion inter-

mediate with interfacial topology (*6*) and suggest that the four helical regions flanking translocating sites might insert cooperatively (compare the topology of residues 162 and 251 in various samples in Table 1). In addition, these data identify the previously unknown TM segment of inserted ANX flanked by residues 221 and 251.

DISCUSSION

FCS and Quantitation of Membrane Partitioning. There are two principal ways of extracting quantitative information on membrane binding from the FCS data. The first method (based on eq 4B and illustrated in Figure 3) relies on the comparison of amplitudes in two protein samples, one in the absence and one in the presence of LUV (*12*). It is essential that the samples have exactly the same concentration of the protein, which is not an easy task to accomplish, as membrane samples are notorious for variation in protein concentration due to precipitation and absorption to the surfaces. Another limitation of this approach is an increasing uncertainty at saturation of binding, as the fraction of the free protein is reduced drastically, and as a result, the autocorrelation amplitudes do not change appreciably.

An alternative approach, introduced here and illustrated in Figure 2, is based on the simplified mathematical treatment (eq 4A) justified under conditions of the so-called infinite dilution regime. These conditions are met when no more than one protein binds to a single vesicle, which in the case of LUV requires a million-fold molar excess of lipid over bound protein [the use of the smaller sonicated vesicles should be avoided, as they are metastable and known to produce anomalous binding (*20, 25, 26*), due perhaps to distorted lipid packing associated with high surface curvature]. Because of the extremely high sensitivity of the FCS experiment, reliable data can be obtained in this concentration range. The main advantage of this approach lies in the fact that a single autocorrelation curve, measured at a particular lipid concentration, contains all of the information needed to calculate free and bound protein fractions. Of course, the most reliable way to extract this information is to compare several data sets, collected at different lipid concentrations or pH (as done here), and to analyze them together using some sort of a linked analysis (Figure 2). But in this case the samples are not required to have exactly the same protein concentration, and the fractions of free and bound protein can be calculated from the normalized autocorrelation curves. The disadvantage of the new approach lies in the stringent requirements of the infinite dilution regime, which makes measurements extremely difficult when lipid concentration is below 50 μM. Nevertheless, our data indicate that both approaches are in excellent agreement when comparable conditions are used (compare solid and open symbols in Figure 4).

Interfacial State and Bilayer Insertion Reaction. Understanding the energetics of protein−membrane interactions is crucial for deciphering the problem of membrane protein stability and, ultimately, for predicting structure from sequence. Most of the methods for experimental determination of protein stability, developed for soluble proteins, are not directly applicable to membrane proteins, especially when they are inserted into lipid membranes. White and co-workers had suggested an alternative approach which relies on the use of membrane interactions of short soluble peptides (*9, 10*). While this approach proved extremely useful for studying thermodynamics of interfacial binding (*27–29*) and folding (*30, 31*), deciphering the energetics of transbilayer insertion turned out to be much more elusive. A study of membrane interactions of a designed peptide TMX-3 (*32*) demonstrated that the interfacial folded state is the most thermodynamically stable state for a self-inserting peptide. This trend cannot be reversed by an increase in sequence hydrophobicity, because the latter results in peptide precipitation in solution (rendering thermodynamic analysis impossible) prior to any noticeable increase in insertion. Consequently, many important thermodynamic parameters, such as the free energy cost for backbone partitioning of the helical segment, crucial for correct prediction of the TM regions (*10*), could not be verified experimentally.

To circumvent this limitation, we have switched from peptides to more complex protein systems [e.g., ANX and diphtheria toxin T-domain (*33–35*)] to study the energetics of membrane insertion. The lessons learned from peptide work, however, are essential to understanding the thermodynamics and molecular mechanisms of pH-triggered insertion/refolding of the T-domain and ANX. The general concept emerging from the peptide studies and from structural studies of the lipid bilayer (*36, 37*) is that the interfacial region of the bilayer can provide special accommodation for large elements of the protein structure undergoing refolding and serve as a catalyst for the conformational change resulting in transbilayer insertion. As a result, any theoretical or experimental description of membrane protein insertion has to explicitly consider both interfacial and transmembrane states.

Several studies of bacterial toxins, colicins, and other spontaneously inserting nonconstitutive proteins (i.e., those not using translocon machinery to get into the bilayer) suggested that an interfacial intermediate state is an important feature of their insertion pathway (*33, 38–40*), a feature also shared by ANX (*6*). None of these studies, however, contained direct kinetic measurements of bilayer topology, defined as *cis* or *trans* location of a particular site of the protein inserting into the lipid bilayer. Recently, we have advanced our original LysoUB topology method (*6*) to take advantage of the fluorescence lifetime measurements (*14*). This allowed us to reduce the data acquisition time from half an hour to several minutes and opened the door to direct probing of the topology of the insertion intermediate, presented here. Our results indicate that residues 134 and 221 remain on the *cis* side at all times, while residues 162 and 251 are rapidly translocated in 75PC:25PG LUV. The use of LUV with an increased content of anionic lipids hinders the translocation (Table 1, Figure 7), which confirms our early suggestion as to the existence of a kinetic insertion intermediate with interfacial topology (*6*).

Comparison of our experimental topology results (stars, Figure 6) with our standard low pH hydropathy prediction (black bars, Figure 6) reveals that an additional TM segment has to be located between the *trans*-162 site and *cis*-221 site. Indeed, this segment can be predicted (orange bar in Figure 6) if we assume that the two histidine residues, H205 and H209, are uncharged (dotted orange hydropathy line). While acidic pH favors protonation of histidines, it is not unusual to see their pK_a shifted down in a nonpolar environment. On the other hand, favorable interaction of protonated

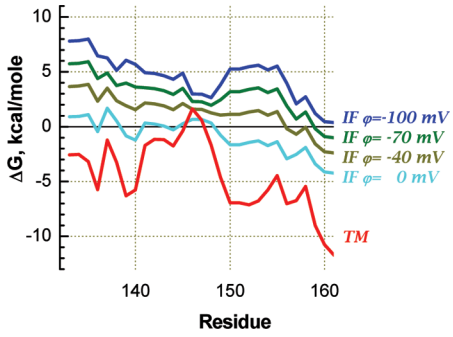

FIGURE 8: Hydropathy analysis illustrating the origins of variations in the topology of the E−D helical region of repeat two of ANX in bilayers of different lipid content. The red curve corresponds to TM prediction; the other curves correspond to IF prediction for membranes with various surface potentials, φ (see text for details).

histidines with anionic lipid headgroups could explain the observed stabilization for the interfacial intermediate (see discussion below). Moreover, even if those residues are still charged, they can lower the penalty for TM penetration by forming salt bridges or, since ANX forms an aqueous pore, by solvation with water. Possibly the segments identified by hydropathy analysis are the first to adopt a TM conformation, while other, less hydrophobic ones [e.g., the one centered at T262 (*24*)] will follow with the formation of an aqueous pore. Therefore, application of hydropathy analysis to nonconstitutive proteins should be done with caution. We use it here to guide the experimental determination of insertion of critical sites.

As discussed above, the interfacial state of ANX is populated as a kinetic intermediate on the pathway toward the fully inserted state. This intermediate can be stabilized by increasing content in anionic lipids, so in 25PC:75PG LUV ANX does not fully translocate across the lipid bilayer even after hours of incubation, while in 75PC:25PG LUV the translocation is completed on a time scale of minutes. A plausible explanation for this hindered insertion is presented in Figure 8, which contains hydropathy analysis for the known TM segment of ANX. The red line corresponds to the TM prediction based on the Wimley−White octanol hydrophobicity scales (*27*), which was shown empirically to give excellent predictions when tested against a database of known TM helixes (*41*). The cyan line corresponds to the IF prediction based on the interfacial Wimley−White scale (*27*) for uncharged bilayer. Other IF lines were generated by addition of the free energy component accounting for electrostatic interactions of the charged residues (most importantly R149) with the membrane of various surface potentials (for details of this analysis see ref *33*). Although a direct comparison of the TM and IF profiles is complicated by a number of factors [most notably by the difference in the reference state and interfacial folding (*33*) and the possible lack of additivity of hydrophobic and electrostatic interactions on membrane interfaces (*28, 42*)], the trend is clear: increasing surface potential will tend to stabilize the IF state over the TM state.

ANX as a Model for Thermodynamic Studies of Membrane Protein Insertion/Folding. While the physiological relevance of the Ca^{2+}-independent TM insertion of ANX at low pH remains under discussion, its role as a model for pH-triggered membrane insertion of bacterial toxins and colicins should not be underestimated. What makes ANX such a convenient model? In addition to the reversible nature of its insertion (*7*), ANX follows a relatively simple insertion pathway. First, ANX will not interact with membranes at neutral pH (in the absence of Ca^{2+}), and second, ANX remains monomeric in solution at low pH (*7*). This distinguishes ANX, for example, from the diphtheria toxin T-domain (*33, 34*) and makes the thermodynamic analysis more straightforward (Figure 1).

Our data presented here indicate that the formation of the membrane-competent state of ANX depends on the protonation near the membrane interface, rather than in the bulk of the solution. This conclusion is based on the fact that the pH titration curves determined at lipid saturation for the two lipid compositions (75PC:25PG and 25PC:75PG) coincide after correction for surface-induced variation in pH (Figure 5A). The resulting titration curve has a pK = 4.3 and the Hill coefficient of $n \sim 2$, indicating titration of two amino acid residues. The free energy of subsequent insertion of ANX across the bilayer is also pH-dependent (Figures 4 and 5B), suggesting change in protonation of additional protein groups at this step. The nature of the titratable residues involved in the two transitions in Figure 1 will be a subject of future studies, involving site-directed mutagenesis. Usually Glu's and Asp's are considered to be crucial for bilayer insertion under acidic conditions; the involvement of His's, however, cannot be ruled out, especially at the first step of formation of the membrane-competent state. Protonation of His residues may be involved in destabilization of the folded ANX in solution, as well as in the promotion of the interfacial state via electrostatic interactions with anionic lipids [e.g., both were suggested for the diphtheria toxin T-domain (*33, 40*)].

Different stages of the pH-triggered insertion pathway of ANX, along with their corresponding time scales, are summarized in Figure 9. A fast transition from the water-soluble W-state to an interfacial intermediate I-state (<10 s (*6*)) is followed by a slower insertion to a final TM T-state. The rate of the latter process is strongly slowed by a high content of anionic lipids, presumably via stabilization of an I-state with Coulombic attraction between anionic lipids and cationic protein groups. If enough protein lingers in the I-state, it starts aggregating (A-state) (*43*), while the properly inserted T-state shows no signs of aggregation in the same concentration range (*7, 43*). At the present time we do not understand what forces contribute to this selective aggregation of the noninserted ANX, but the nature of the interfacial zone of the lipid bilayer is bound to play a role (*10, 44*).

Application of the FCS methodology had permitted accurate determination of the free energy of transfer of ANX from solution into the lipid bilayer. Numerous data from our laboratory and others indicate transmembrane topology of the ANX (*5, 6, 24*), especially in the 75PC:25PG LUV (Table 1). Thus the goal of accurate thermodynamic measurement of the ΔG for TM insertion motivating this study has been achieved, and ANX can now be used as a template for further host–guest mutagenesis studies. As revealed by our kinetic topology studies, the insertion into 25PC:75PG LUV is slow; therefore, the free energy of 11–12 kcal/mol measured with this lipid composition corresponds to the transfer to the IF state, ΔG^{IF}. For the 75PC:25PG LUV the insertion is very fast, and the free energy of 10–11 kcal/mol, for the comparable pH range, corresponds to the TM state, ΔG^{TM}. Let us consider that the ΔG^{TM} does not depend on the surface

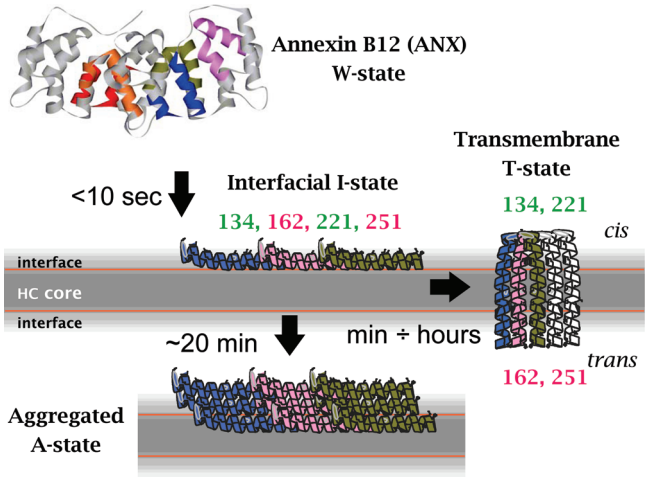

FIGURE 9: Schematic representation of the insertion pathway of ANX into the lipid bilayer at low pH, containing the water-soluble state (W), final transmembrane state (T), interfacial intermediate state (I), and aggregated state (A). The initial unfolding (W to I) occurs very fast (*6*), while the final insertion (I to T), resulting in translocation of several helical hairpins (residues 162 and 251), may take somewhere from minutes to hours (Table 1), depending on the lipid composition. An excess of anionic lipids will stabilize the insertion intermediate (ref *6* and this paper) which at high concentrations is prone to aggregation on the time scale of tens of minutes (*43*). Formation of a membrane-competent form of ANX is likely to occur in close proximity to the membrane interface and requires protonation of two residues (Figure 5A), while additional protonation may be required for bilayer insertion (Figure 5B). The free energies for final insertion ΔG^{TM} (W to T) and interfacial penetration (W to I) ΔG^{IF} have similar values, ~10–12 kcal/mol; thus the final transmembrane insertion is affected by a complex interplay of electrostatic and hydrophobic interactions.

potential, while the ΔG^{IF} obviously does (Figure 6). The difference in the surface potential between the two lipid systems in this study is ~30 mV [−105 mV for 25PC:75PG and –74 mV for 75PC:25PG (*42*)], meaning that just four positive charges will be sufficient to bring an additional ~3 kcal/mol to the IF state in 25PC:75PG. For example, R149, R199, H205, and H209 are located in the segments that can undergo a TM insertion in ANX (Figure 6, Table 1, and refs *5* and *6*), and therefore their electrostatic attraction to the anionic membrane interface will be sufficient to make the IF conformation more favorable compared to the TM. The small difference between the energy levels of TM and IF means that the insertion is fine-tuned for a particular surface potential, as observed for example with colicin E1 (*45*).

Improving existing prediction algorithms for membrane interactions from genomic data requires further refinement of the physicochemical rules for quantifying various factors influencing the transitions to interfacial and to the final inserted state. Nevertheless, it is clear that the interfacial state should be considered explicitly in predicting membrane association of nonconstitutive proteins, such as bacterial toxins, colicins, or annexins (*33, 39, 40, 45*). The interfacial interactions, however, are important not only for these proteins but also for those involved in cell signaling (*46*), enzymatic surface activity [e.g., phospholipases (*47*)], host-defense function [peptide antibiotics (*48, 49*)], membrane fusion [e.g., "membrane-dipped" parts of the neuronal SNARE complex (*50, 51*) or influenza hemagglutinin (*52*)], and the action of ion-channel blockers (*53–55*). Moreover, recent studies of the thermodynamics of cotranslational membrane protein insertion (*1*) suggest that protein–lipid interactions may determine the recognition of TM helices at the ER translocon (*2, 3*). This suggests the intriguing but poorly explored possibility of a link between disease-associated membrane protein misfolding (*56*) and the relative stability of the interfacial (misfolded) state of native TM segments of constitutive proteins.

ACKNOWLEDGMENT

We are grateful to Mr. M. A. Myers for editorial help and to Dr. H. T. Haigler for the gift of ANX mutants.

REFERENCES

1. Hessa, T., Kim, H., Bihlmaler, K., Lundin, C., Boekel, J., Andersson, H., Nilsson, I., White, S. H., and von Heijne, G. (2005) Recognition of transmembrane helices by the endoplasmic reticulum translocon. *Nature 433*, 377–381.
2. White, S. H., and von Heijne, G. (2005) Do protein-lipid interactions determine the recognition of transmembrane helices at the ER translocon? *Biochem. Soc. Trans. 33*, 1012–1015.
3. Bowie, J. U. (2005) Border crossing. *Nature 433*, 367–369.
4. Swairjo, M. A., and Seaton, B. A. (1994) Annexin structure and membrane interactions: A molecular perspective. *Annu. Rev. Biophys. Biomol. Struct. 23*, 193–213.
5. Langen, R., Isas, J. M., Hubbell, W. L., and Haigler, H. T. (1998) A transmembrane form of annexin XII detected by site-directed spin labeling. *Proc. Natl. Acad. Sci. U.S.A. 95*, 14060–14065.
6. Ladokhin, A. S., Isas, J. M., Haigler, H. T., and White, S. H. (2002) Determining the membrane topology of proteins: Insertion pathway of a transmembrane helix of annexin 12. *Biochemistry 41*, 13617–13626.
7. Ladokhin, A. S., and Haigler, H. T. (2005) Reversible transition between the surface trimer and membrane-inserted monomer of annexin 12. *Biochemistry 44*, 3402–3409.
8. Renthal, R. (2006) An unfolding story of helical transmembrane proteins. *Biochemistry 45*, 14559–14566.
9. White, S. H., Wimley, W. C., Ladokhin, A. S., and Hristova, K. (1998) Protein folding in membranes: Determining the energetics of peptide-bilayer interactions. *Methods Enzymol. 295*, 62–87.
10. White, S. H., Ladokhin, A. S., Jayasinghe, S., and Hristova, K. (2001) How membranes shape protein structure. *J. Biol. Chem. 276*, 32395–32398.
11. Haustein, E., and Schwille, P. (2003) Ultrasensitive investigations of biological systems by fluorescence correlation spectroscopy. *Methods 29*, 153–166.
12. Rusu, L., Gambhir, A., McLaughlin, S., and Radler, J. (2004) Fluorescence correlation spectroscopy studies of peptide and protein binding to phospholipid vesicles. *Biophys. J. 87*, 1044–1053.
13. Rhoades, E., Ramlall, T. F., Webb, W. W., and Eliezer, D. (2006) Quantification of alpha-synuclein binding to lipid vesicles using fluorescence correlation spectroscopy. *Biophys. J. 90*, 4692–4700.
14. Posokhov, Y. O., and Ladokhin, A. S. (2006) Lifetime fluorescence method for determining membrane topology of proteins. *Anal. Biochem. 348*, 87–93.
15. Hope, M. J., Bally, M. B., Mayer, L. D., Janoff, A. S., and Cullis, P. R. (1986) Generation of multilamellar and unilamellar phospholipid vesicles. *Chem. Phys. Lipids 40*, 89–107.
16. Mayer, L. D., Hope, M. J., and Cullis, P. R. (1986) Vesicles of variable sizes produced by a rapid extrusion procedure. *Biochim. Biophys. Acta 858*, 161–168.
17. Bartlett, G. R. (1959) Phosphorus assay in column chromatography. *J. Biol. Chem. 234*, 466–468.
18. Hess, S. T., Huang, S., Heikal, A. A., and Webb, W. W. (2002) Biological and chemical applications of fluorescence correlation spectroscopy: A review. *Biochemistry 41*, 697–705.
19. Clamme, J. P., Azoulay, J., and Mely, Y. (2003) Monitoring of the formation and dissociation of polyethylenimine/DNA complexes by two photon fluorescence correlation spectroscopy. *Biophys. J. 84*, 1960–1968.
20. Ladokhin, A. S., Jayasinghe, S., and White, S. H. (2000) How to measure and analyze tryptophan fluorescence in membranes properly, and why bother? *Anal. Biochem. 285*, 235–245.

21. Fernandez, M. S., and Fromherz, P. (1977) Lipoid pH indicators as probes of electrical potential and polarity in micelles. *J. Phys. Chem. 81*, 1755–1761.
22. Knutson, J. R., Beechem, J. M., and Brand, L. (1983) Simultaneous analysis of multiple fluorescence decay curves: A global approach. *Chem. Phys. Lett. 102*, 501–507.
23. Beechem, J. M., Ameloot, M., and Brand, L. (1985) Global and target analysis of complex decay phenomena. *Anal. Instrum. 14*, 379–402.
24. Kim, Y. E., Isas, J. M., Haigler, H. T., and Langen, R. (2005) A helical hairpin region of soluble annexin B12 refolds and forms a continuous transmembrane helix at mildly acidic pH. *J. Biol. Chem. 280*, 32398–32404.
25. Greenhut, S. F., Bourgeois, V. R., and Roseman, M. A. (1986) Distribution of cytochrome b_5 between small and large unilamellar phospholipid vesicles. *J. Biol. Chem. 261*, 3670–3675.
26. Seelig, J., and Ganz, P. (1991) Nonclassical hydrophobic effect in membrane binding equilibria. *Biochemistry 30*, 9354–9359.
27. Wimley, W. C., and White, S. H. (1996) Experimentally determined hydrophobicity scale for proteins at membrane interfaces. *Nat. Struct. Biol. 3*, 842–848.
28. Ladokhin, A. S., and White, S. H. (2001) Protein chemistry at membrane interfaces: Non-additivity of electrostatic and hydrophobic interactions. *J. Mol. Biol. 309*, 543–552.
29. Hristova, K., and White, S. H. (2005) An experiment-based algorithm for predicting the partitioning of unfolded peptides into phosphatidylcholine bilayer interfaces. *Biochemistry 44*, 12614–12619.
30. Ladokhin, A. S., and White, S. H. (1999) Folding of amphipathic α-helices on membranes: Energetics of helix formation by melittin. *J. Mol. Biol. 285*, 1363–1369.
31. Fernandez-Vidal, M., Jayasinghe, S., Ladokhin, A. S., and White, S. H. (2007) Folding amphipathic helices into membranes: amphiphilicity trumps hydrophobicity. *J. Mol. Biol. 370*, 459–470.
32. Ladokhin, A. S., and White, S. H. (2004) Interfacial folding and membrane insertion of a designed helical peptide. *Biochemistry 43*, 5782–5791.
33. Ladokhin, A. S., Legmann, R., Collier, R. J., and White, S. H. (2004) Reversible refolding of the diphtheria toxin T-domain on lipid membranes. *Biochemistry 43*, 7451–7458.
34. Palchevskyy, S. S., Posokhov, Y. O., Olivier, B., Popot, J. L., Pucci, B., and Ladokhin, A. S. (2006) Chaperoning of insertion of membrane proteins into lipid bilayers by hemifluorinated surfactants: Application to diphtheria toxin. *Biochemistry 45*, 2629–2635.
35. Rodnin, M. V., Posokhov, Y. O., Contino-Pepin, C., Brettmann, J., Kyrychenko, A., Palchevskyy, S. S., Pucci, B., and Ladokhin, A. S. (2008) Interactions of fluorinated surfactants with diphtheria toxin T-domain: Testing new media for studies of membrane proteins. *Biophys. J.* 94.
36. Wiener, M. C., and White, S. H. (1992) Structure of a fluid dioleoylphosphatidylcholine bilayer determined by joint refinement of x-ray and neutron diffraction data. III. Complete structure. *Biophys. J. 61*, 434–447.
37. White, S. H., and Wiener, M. C. (1995) Determination of the structure of fluid lipid bilayer membranes, in *Permeability and Stability of Lipid Bilayers* (Disalvo, E. A., and Simon, S. A., Eds.) pp 1–19, CRC Press, Boca Raton, FL.
38. Zakharov, S. D., Lindeberg, M., and Cramer, W. A. (1999) Kinetic description of structural changes linked to membrane import of the colicin E1 channel protein. *Biochemistry 38*, 11325–11332.
39. Wang, Y., Malenbaum, S. E., Kachel, K., Zhan, H. J., Collier, R. J., and London, E. (1997) Identification of shallow and deep membrane-penetrating forms of diphtheria toxin T domain that are regulated by protein concentration and bilayer width. *J. Biol. Chem. 272*, 25091–25098.
40. Perier, A., Chassaing, A., Raffestin, S., Pichard, S., Masella, M., Menez, A., Forge, V., Chenal, A., and Gillet, D. (2007) Concerted protonation of key histidines triggers membrane interaction of the diphtheria toxin T domain. *J. Biol. Chem. 282*, 24239–24245.
41. Jayasinghe, S., Hristova, K., and White, S. H. (2001) Energetics, stability, and prediction of transmembrane helices. *J. Mol. Biol. 312*, 927–934.
42. Posokhov, Y. O., Gottlieb, P. A., Morales, M. J., Sachs, F., and Ladokhin, A. S. (2007) Is lipid bilayer binding a common property of inhibitor cysteine knot ion-channel blockers? *Biophys. J. 93*, L20–2.
43. Ladokhin, A. S. (2008) Insertion intermediate of annexin B12 is prone to aggregation on membrane interfaces. *Biopolym. Cell 24*, 101–104.
44. Wimley, W. C., Hristova, K., Ladokhin, A. S., Silvestro, L., Axelsen, P. H., and White, S. H. (1998) Folding of β-sheet membrane proteins: A hydrophobic hexapeptide model. *J. Mol. Biol. 277*, 1091–1110.
45. Zakharov, S. D., Heymann, J. B., Zhang, Y.-L., and Cramer, W. A. (1996) Membrane binding of the colicin E1 channel: Activity requires an electrostatic interaction of intermediate magnitude. *Biophys. J. 70*, 2774–2783.
46. McLaughlin, S., and Murray, D. (2005) Plasma membrane phosphoinositide organization by protein electrostatics. *Nature 438*, 605–611.
47. Ghomashchi, F., Lin, Y., Hixon, M. S., Yu, B.-Z., Annand, R., Jain, M. K., and Gelb, M. H. (1998) Interfacial recognition by bee venom phospholipase A_2: Insights into nonelectrostatic molecular determinants by charge reversal mutagenesis. *Biochemistry 37*, 6697–6710.
48. Zasloff, M. (2002) Antimicrobial peptides of multicellular organisms. *Nature 415*, 389–395.
49. Shai, Y. (2002) Mode of action of membrane active antimicrobial peptides. *Biopolymers 66*, 236–248.
50. Kim, C. S., Kweon, D.-H., and Shin, Y.-K. (2002) Membrane topologies of neuronal SNARE folding intermediates. *Biochemistry 41*, 10928–10933.
51. Kweon, D.-H., Kim, C. S., and Shin, Y.-K. (2002) The membrane-dipped neuronal SNARE complex: A site-directed spin labeling electron paramagnetic resonance study. *Biochemistry 41*, 9264–9268.
52. Tamm, L. K., Han, X., Li, Y., and Lai, A. L. (2002) Structure and function of membrane fusion peptides. *Biopolymers 66*, 249–260.
53. Lee, S.-Y., and MacKinnon, R. (2004) A membrane-access mechanism of ion channel inhibition by voltage sensor toxins from spider venom. *Nature 430*, 232–240.
54. Suchyna, T. M., Tape, S. E., Koeppe, R. E., Anderson, O. S., Sachs, F., and Gottlieb, P. A. (2004) Bilayer-dependent inhibition of mechanosensitive channels by neuroactive peptide enantiomers. *Nature 430*, 235–240.
55. Garcia, M. L. (2004) Ion channels: Gate expectations. *Nature 430*, 153–155.
56. Sanders, C. R., and Nagy, J. K. (2000) Misfolding of membrane proteins in health and disease: The lady or the tiger? *Curr. Opin. Struct. Biol. 10*, 438–442.
57. Magde, D., Elson, E. L., and Webb, W. W. (1974) Fluorescence correlation spectroscopy. II. An experimental realization. *Biopolymers 13*, 29–61.

BI702223C